A viscoelastic damage model with applications to stable and unstable fracturing

Yariv Hamiel,[1,2] Yunfeng Liu,[3] Vladimir Lyakhovsky,[2] Yehuda Ben-Zion[3] and David Lockner[4]

[1]*Institute of Earth Sciences, Hebrew University of Jerusalem, Jerusalem* 91904 *Israel. E-mail: yarivh@cc.huji.ac.il*
[2]*Geological Survey of Israel, Jerusalem* 95501, *Israel*
[3]*Department of Earth Sciences, University of Southern CA, Los Angeles,* CA 90089-0740, *USA*
[4]*U.S.G.S.,* MS 977, 345 *Middlefield Rd., Menlo Park,* CA 94025, *USA*

SUMMARY

A viscoelastic damage rheology model is presented that provides a generalization of Maxwell viscoelasticity to a non-linear continuum mechanics framework incorporating material degradation and recovery, transition from stable to unstable fracturing and gradual accumulation of non-reversible deformation. The model is a further development of the damage rheology framework of Lyakhovsky *et al.* for evolving effective elasticity. The framework provides a quantitative treatment for macroscopic effects of evolving distributed cracking with local density represented by an intensive state variable. The formulation, based on thermodynamic principles, leads to a system of kinetic equations for the evolution of damage. An effective viscosity inversely proportional to the rate of damage increase is introduced to account for gradual accumulation of irreversible deformation due to dissipative processes. A power-law relation between the damage variable and elastic moduli leads to a non-linear coupling between the rate of damage evolution and the damage variable itself. This allows the model to reproduce a transition from stable to unstable fracturing of brittle rocks and the Kaiser effect. 3-D numerical simulations based on the model formulation for homogeneous and heterogeneous materials account for the main features of rock behaviour under large strain. The model coefficients are constrained, using triaxial laboratory experiments with low-porosity Westerly granite and high-porosity Berea sandstone samples.

Key words: cracked media, rheology, viscoelasticity.

GJI Volcanology, geothermics, fluids and rocks

1 INTRODUCTION

Fracture processes control the mechanical response and stability of a rock mass under brittle conditions and produce rock damage. The evolving rock damage in turn modifies the strength and elastic properties of the rock (e.g. Nishihara 1957; Zoback & Byerlee 1975; Schock 1977; Lockner & Byerlee 1980; Schock & Louis 1982; Alm *et al.* 1985; Reches & Lockner 1994; Weinberger *et al.* 1994; Pestman & Munster 1996) and leads to reduced elastic moduli at large stresses before brittle failure (e.g. Lockner & Byerlee 1980; Lockner *et al.* 1991, 1992). Laboratory investigations of rock fracturing show that this process cannot be described in terms of propagation of a single crack in the framework of linear elastic fracture mechanics (e.g. Yukutake 1989; Lockner *et al.* 1991, 1992; Reches & Lockner 1994). The distributed damage at the tip of a propagating crack, or process zone, is often treated by models that specify a cohesive zone within the plane of the crack, which eliminates the non-physical crack-tip singularity (e.g. Dugdale 1960; Barenblatt

1962; Ida 1972; Palmer & Rice 1973; Rubin 1993, 1995; Willemse & Pollard 1998). The size and geometry of the damage zone control both the trajectory and growth rate of the evolving macrocrack (Bazant & Cedolin 1991; Huang *et al.* 1991; Chai 1993; Zietlow & Labuz 1998). Thus it is important to account explicitly for the distribution of damage in analysis of rock fracturing.

The theory of damage mechanics has been applied extensively to model fracturing processes in engineering and rock-like materials. In this theory, the degradation of elastic moduli and strength of the material is interpreted as resulting from an increase in the density of cracks or rock damage. In order to simulate this degradation, a non-dimensional intensive damage variable α is introduced. In continuum frameworks, the damage variable characterizes rock volumes large enough that the distribution of internal flaws (microcracks in laboratory specimens or small faults in a crustal domain) continues smoothly. Therefore, the continuum damage mechanical approach does not imply precise micromechanical fracture mechanisms. The effect of rock degradation is achieved by making the elastic moduli

a decreasing function of the damage variable. Several researchers (see, e.g., the review of Kachanov 1994) have proposed models with a scalar damage variable that fit various aspects of existing experimental results. In the study of Hansen & Schreyer (1994), a scalar isotropic damage model correlated well with changes in Young's modulus but not with changes in the apparent Poisson ratio. For this reason, Ju (1990) and Hansen & Schreyer (1994) suggested upgrading the damage variable from a scalar to a tensor quantity. Such a tensorial damage model contains at least three adjustable parameters that can be used to simulate the evolution of the apparent Poisson ratio. Variations of Young's modulus and Poisson's ratio with damage intensity under different types of load can also be described using a non-linear elastic model with a scalar damage variable. This was done in the thermodynamically based damage model proposed by Lyakhovsky & Myasnikov (1984), Agnon & Lyakhovsky (1995) and Lyakhovsky *et al.* (1997a,b).

For mathematical simplicity, the damage model of Lyakhovsky *et al.* (1997a) ignores gradual accumulation of irreversible strain before the free energy function loses its convexity and a macroscopic brittle failure occurs. Ben-Zion *et al.* (1999), Lyakhovsky *et al.* (2001) and Ben-Zion & Lyakhovsky (2002) use the loss of convexity of the energy function to define initiation of seismic events associated with a step-like increase of inelastic strain in regional lithospheric models incorporating the damage rheology. Fig. 1 shows schematically stress–strain relations for linear elasticity and elastic and viscoelastic damage rheology models. Deformation of a damage-free rock follows linear Hookean elasticity represented by a dotted line. The stress–strain curve begins to deviate from linear elasticity when the conditions for the onset of damage evolution are achieved (point A in Fig. 1). The stage of distributed damage increase begins with the onset of damage and ends at point C, where brittle failure of the rock occurs. If the loading is stopped at point B, the elastic damage model reverts to zero total strain after unloading the stress to zero, by a different path, as shown in Fig. 1. The area between the loading and unloading paths (area 1 in Fig. 1) represents

energy dissipated due to the creation of damage and friction between crack surfaces during the cycle (Jaeger & Cook 1984). Rocks exhibit a more complex behaviour and the strain during unloading beyond point A does not return to zero but to a permanent inelastic strain level ε_0^i. The accumulation of an additional irreversible strain component slightly changes the new loading path (curve A–B′–C′ instead of A–B–C in Fig. 1). An extra energy dissipated during the loading cycle (the difference between areas 2 and 1 in Fig. 1) is related to permanent inelastic slip between the microcrack surfaces. In this paper we attribute that permanent strain and additional dissipation to a damage-related viscosity in a viscoelastic version of the damage rheology model.

The generalized formulation presented provides a better agreement between model predictions and observed features of rock mechanics experiments, including the onset of brittle failure, stable/unstable fracturing and the Kaiser effect. Stable fracturing is a situation in which an increase of load is required to cause further cracking, whereas in the unstable regime no further increase of load is required for a complete eventual failure of the sample (Bieniawski 1967). The unstable crack growth and static fatigue were related experimentally by Martin & Chandler (1994) to situations where the time-to-failure under constant loading is finite. According to static fatigue tests, the stress at failure decreases with an increase in the loading time (e.g. Kranz *et al.* 1982; Lawn 1993; Bolotin 1999). Under cyclical load, acoustic emissions are not created at stress levels less than the maximum stress reached in the previous cycle, while above that level there is a high production of additional acoustic emissions. Although this stress-memory effect, called the Kaiser effect, was discovered more than 50 yr ago (Kaiser 1950), it is not well understood theoretically, especially for rocks (Holcomb 1993; Tang *et al.* 1997; Lavrov 2001).

In the following sections we first discuss the theoretical basis for the elastic and viscoelastic versions of our damage rheology model. Then we apply the damage rheology model to laboratory triaxial experiments with low-porosity Westerly granite and high-porosity
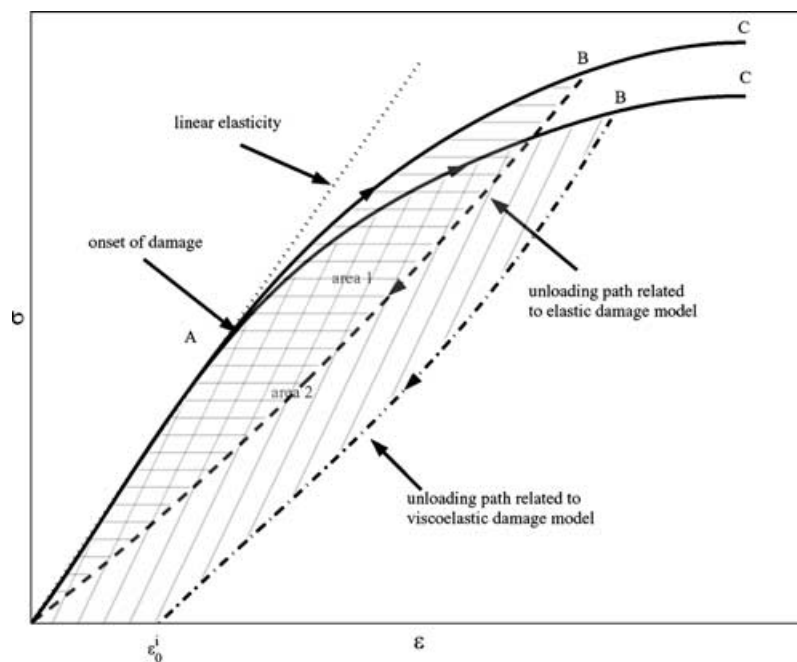

Figure 1. Schematic diagram of stress–strain relations and related energy partitions for linear elasticity, the pure elastic damage model (Lyakhovsky *et al.* 1997a) and the viscoelastic model (the present model). The areas between the loading and unloading paths represent energy dissipation in the pure elastic damage model (area 1, horizontal lines) and in the present model (area 2, diagonal lines).

Berea sandstone samples. The quantities measured in the laboratory experiments are axial and transverse components of stress–strain curves and acoustic emissions. Some of the experiments included small loading–unloading cycles during which the Kaiser effect was observed. Using a simplified analysis for a homogeneous distribution of damage (single-element simulation) and 3-D numerical simulations accounting for spatial heterogeneity in damage evolution, we show that the viscoelastic version of the model can account quantitatively for the main stages and key deformation features of the various experiments.

2 THEORY

In this section we present the main features of the damage rheology model. To evaluate the damage effects, Lyakhovsky *et al.* (1997b) derived the macroscopic stress–strain relations for a 3-D elastic solid with non-interacting cracks embedded inside a homogeneous matrix. The assumed cracks dilate due to local tension perpendicular to the crack orientation or contract under local compression. The solution for the elastic energy of such a solid was derived using the self-consistent scheme of Budiansky & O'Connell (1976). Following the formulations discussed by Lyakhovsky *et al.* (1997a,b), the elastic potential can be written as a second-order non-analytical function of the strain invariants:

$$U = \frac{1}{\rho}\left(\frac{\lambda}{2}I_1^2 + \mu I_2 - \gamma I_1 \sqrt{I_2}\right), \tag{1}$$

where ρ is the density, λ and μ are the Lamé parameters and $I_1 = \varepsilon_{ii}$ and $I_2 = \varepsilon_{ij}\varepsilon_{ij}$ are two independent invariants of the elastic strain tensor. The energy expression (1), adds to the two quadratic terms of the Hookean elastic solid a third non-analytical, second-order term with a coefficient γ. This is the simplest mathematical generalization of the elastic energy that goes beyond the classical form of Hookean elasticity. Energy expressions with non-integer power of state variables are common for many well-known non-linear systems, e.g. Hertzian theory for elastic deformation of a granular medium or van der Waals energy equation for a non-ideal gas. Similarly, the third term in (1) incorporates non-linear elasticity, even for an infinitesimal strain, and it simulates abrupt change in the elastic moduli when the loading reverses from compression to tension. Lyakhovsky *et al.* (1997a) derived the conditions imposed on the elastic moduli λ, μ, and γ to ensure the convexity of the elastic potential (1), and calculated the maximum value of γ using a condition for loss of convexity corresponding to macroscopic brittle failure.

Following Murnaghan (1951), the stress tensor, σ_{ij}, is defined as a derivative of the energy potential (1) with respect to the strain tensor

$$\sigma_{ij} = \rho \frac{\partial U}{\partial \varepsilon_{ij}} = \left(\lambda - \frac{\gamma}{\xi}\right)I_1 \delta_{ij} + 2\left(\mu - \frac{1}{2}\gamma\xi\right)\varepsilon_{ij}, \tag{2}$$

where $\xi = I_1/\sqrt{I_2}$, referred to as the strain diagonality, varies from $-\sqrt{3}$ for pure compaction to $+\sqrt{3}$ for pure tension. A value of $\xi = 0$ corresponds to pure shear or zero volumetric strain ($I_1 = 0$). A non-zero coupling coefficient γ makes the effective elastic moduli dependent on the strain diagonality ξ.

The kinetic aspect of the damage rheology model is introduced by making the elastic moduli functions of a scalar damage variable α (i.e. $\lambda(\alpha)$, $\mu(\alpha)$ and $\gamma(\alpha)$), with $0 \leq \alpha \leq 1$. For mathematical simplicity we keep one of the elastic moduli constant. Thus, we consider the following three combinations: (i) $\gamma = \text{const.}$, $\lambda = \lambda(\alpha)$, $\mu = \mu(\alpha)$; (ii) $\mu = \text{const.}$, $\lambda = \lambda(\alpha)$, $\gamma = \gamma(\alpha)$; (iii) $\lambda = \text{const.}$,

$\mu = \mu(\alpha)$, $\gamma = \gamma(\alpha)$. All three combinations lead to a decrease in Young's modulus with damage. However, combination (i) preserves a constant Poisson ratio, as discussed by Hansen & Schreyer (1994). In both combinations (ii) and (iii) the Poisson ratio changes, but only combination (iii) leads to an increase in the Poisson ratio and dilatation with increasing damage. An increase in Poisson's ratio, dilation and decrease in Young's modulus are all widely observed features in rock mechanics experiments (e.g. Jaeger & Cook 1984; Martin & Chandler 1994). Having limited observational data, Agnon & Lyakhovsky (1995) assumed that the moduli μ and γ are linear functions of the damage variable α (i.e. $\mu = \mu_0 - \alpha\mu_1$, $\gamma = \alpha\gamma_1$) and the modulus λ is constant. The values of μ_1 and γ_1 were constrained by Lyakhovsky *et al.* (1997a, eq. 15) from the condition of material destruction for $\alpha = 1$. In the present formulation we follow similar assumptions and vary only two of the elastic moduli, but we generalize the relations between the damage variable and elastic moduli to the forms:

$$\lambda = \text{const.}, \quad \mu = \mu_0 - \mu_1 \alpha, \quad \gamma = \gamma_1 \frac{\alpha^{1+\beta}}{1+\beta}, \tag{3}$$

where β is constant. As will be shown later, the choice $0 < \beta < 1$ in conjunction with other model coefficients provides a better fit to experimental data than the previous assumption of $\beta = 0$. In the next section we will use the elastic energy (1) and the elastic moduli for damaged material (3) to derive an equation for damage evolution, and show that it reproduces the transition between stable and unstable weakening and the Kaiser effect.

2.1 Kinetics of damage evolution

The damage evolves with time as a result of the ongoing deformation. Here we briefly present the thermodynamic background of the damage rheology model (see Lyakhovsky *et al.* 1997a, for detailed derivation of the equation of damage evolution). The free energy, $F(T, \varepsilon_{ij}, \alpha) = U - TS$, of a solid is assumed to be a function of temperature, T, elastic strain, ε_{ij}, and damage variable, α. The entropy is given by $S = -\partial F/\partial T$ (Malvern 1969). The assumption that the energy depends only on the elastic strain, $\varepsilon_{ij} = \varepsilon_{ij}^{\text{t}} - \varepsilon_{ij}^{\text{v}}$, i.e. the difference between the total strain, $\varepsilon_{ij}^{\text{t}}$, and the irreversible strain, $\varepsilon_{ij}^{\text{v}}$, is consistent with a viscoelastic Maxwell model. Using the balance equations of the energy and entropy, the Gibbs relation, and the definition (Murnaghan 1951) of the stress tensor (2), the local entropy production, Φ, may be represented as

$$\Phi = -\frac{Q_i}{\rho T}\nabla_i T + \frac{1}{\rho}\sigma_{ij}\frac{d\varepsilon_{ij}^{\text{v}}}{dt} - \frac{\partial U}{\partial \alpha}\frac{d\alpha}{dt} \geq 0, \tag{4}$$

where Q_i is the heat flux. The first term of eq. (4) describes entropy production by heat conduction; the second term is related to viscous dissipation; and the last term is related to internal energy changes caused by microcracking. The elastic deformation is conservative and does not contribute to the entropy production. Each term in eq. (4) represents entropy production due to a different physical process and can be classified according to its tensorial rank (deGroot & Mazur 1962). Therefore, they should provide a non-negative entropy production separately. The phenomenological equations for the kinetics of $\varepsilon_{ij}^{\text{v}}$ and α are written as (deGroot & Mazur 1962; Malvern 1969)

$$\frac{d\varepsilon_{ij}^{\text{v}}}{dt} = \frac{1}{\eta}\sigma_{ij}, \tag{5}$$

$$\frac{d\alpha}{dt} = -C\frac{\partial F}{\partial \alpha}, \tag{6}$$

where the viscosity η and the coefficient C are positive functions of the state variables describing the rate of irreversible strain accumulation and damage processes, respectively. In the case of Maxwell viscoelasticity, the same total stress defines the elastic deformation through the Murnaghan relations (2) and drives the accumulation of the irreversible strain accumulation (5). The damage kinetic eq. (6) describes not only damage increase, but also a process of material recovery associated with healing of microcracks, which is favoured by high confining pressure, low shear stress, and, especially, high temperature. Substituting (1) into (6) using (3), the damage evolution (6) can be rewritten as

$$\frac{d\alpha}{dt} = C_d I_2 \left(\alpha^\beta \xi - \xi_0 \right), \tag{7}$$

where $\xi_0 = \mu_1/\gamma_1$ and the coefficient $C_d > 0$ describes the rate of damage evolution for a given deformation.

In the previous work by Lyakhovsky *et al.* (1997a) with $\beta = 0$ the transition between degradation and healing was assumed to occur at a critical strain-invariant ratio $\xi = \xi_0 < 0$ (Fig. 2a). The coefficient ξ_0 was related to the friction angle (Agnon & Lyakhovsky 1995) and the modulus γ_1 was constrained by the condition for loss of convexity (eqs 14 and 15 in Lyakhovsky *et al.* 1997a). The model version with $\beta = 0$ did not account for possible stable weakening, and once the strain field exceeds ξ_0 unstable weakening of the sample occurred. Hence, the previous formulation cannot reproduce the Kaiser effect. This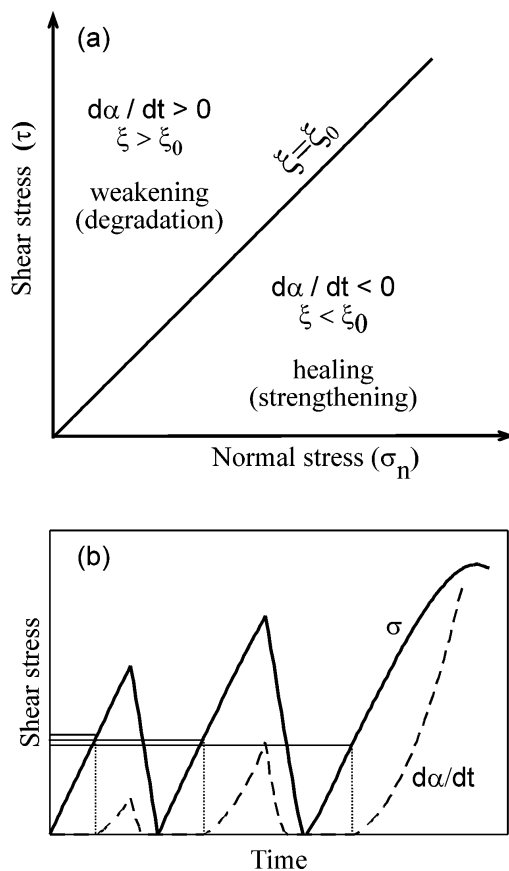 is demonstrated in Fig. 2(b) with a simulation of damage evolution for $\beta = 0$ under cyclic loading. Shear stress was cyclically increased (continuous line in Fig. 2b) due to a constant strain rate applied to initially damage-free material. In every cycle the damage starts to accumulate (broken line in Fig. 2b) at a loading level corresponding to a critical strain-invariant ratio $\xi = \xi_0$. In this case, onset of damage occurs at about the same loading, or even lower, than that of the previous cycle, due to material weakening. This result contradicts the observed Kaiser effect where new acoustic emissions occur only when the stress exceeds the maximum stress of the previous cycle.

The proposed power-law relation (3) between the damage variable and the elastic modulus, γ, leads to a non-linear coupling between the rate of damage evolution and the damage variable itself (7). The steady-state solution ($d\alpha/dt = 0$) of (7) gives a transitional strain-invariant ratio, ξ_{tran}, that separates the healing and stable weakening regions,

$$\xi_{tran}(\alpha) = \frac{\xi_0}{\alpha^\beta}. \tag{8}$$

In the current formulation with $\beta > 0$, three different types of damage evolution exist, shown in Fig. 3(a). The first type is healing or damage decrease for $\xi < \xi_{tran}(\alpha)$. The second type is stable weakening for $\xi_{tran}(\alpha) \leq \xi < \xi_0$. In this region the steady-state solution for damage is a stable value $\alpha \leq 1$, and the damage does not grow to a level of complete failure. The third type is unstable weakening for $\xi \geq \xi_0$. In this regime the steady-state solution for damage is
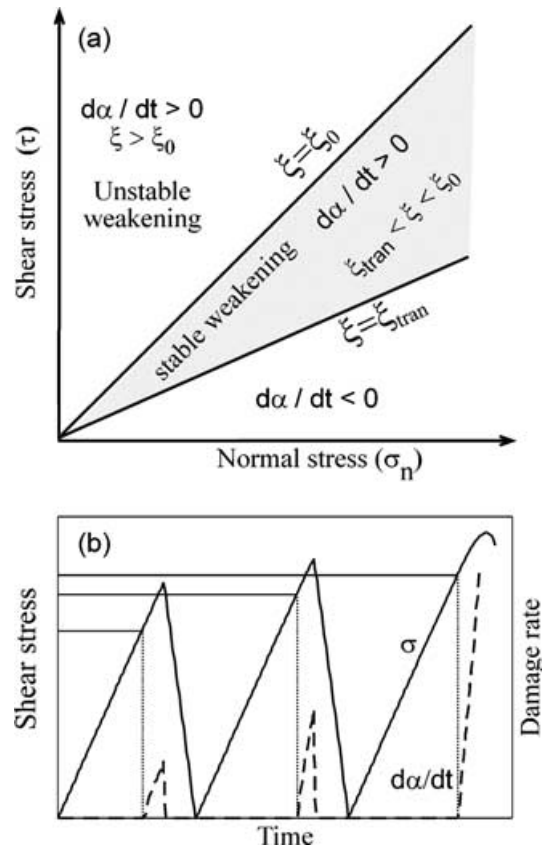

Figure 2. (a) States of stress associated with material weakening (degradation) and healing for model with $\beta = 0$. Degradation ($d\alpha/dt > 0$) occurs whenever $\xi > \xi_0$ and healing, when $\xi < \xi_0$. (b) Schematic cyclic loading and damage rate for simulation with $\beta = 0$ and zero initial damage ($\alpha_0 = 0$).

Figure 3. (a) States of stress associated with unstable and stable material weakening and healing for model with $\beta > 0$ and $\alpha_0 > 0$. Unstable weakening occurs whenever $\xi \geq \xi_0$; stable weakening occurs when $\xi_{tran} \leq \xi < \xi_0$; and healing when $\xi < \xi_{tran}$. (b) Schematic cyclic loading and damage rate for simulation with $\beta = 0.5$ and $\alpha_0 = 0.1$. Note that the damage rate is roughly zero for stresses lower than the maximal stress previously achieved.
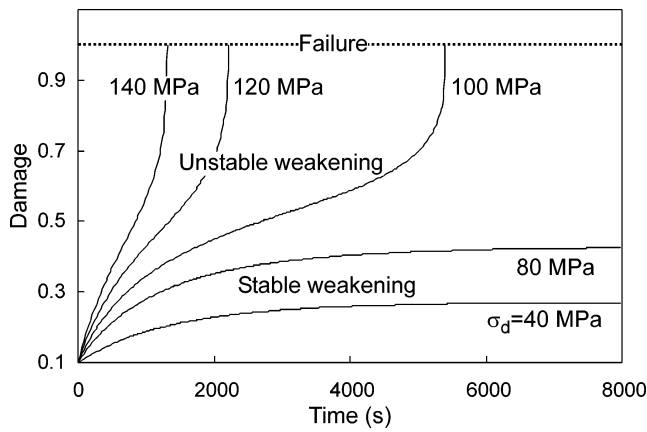
Figure 4. Damage evolution for simulations with constant differential stress, σ_d and confining pressure (50 MPa). The coefficients used in these simulations are the same as the coefficients for BS1 (see Table 1), except that here $C_v = 0$.

unstable, and loading in this region will lead to $\alpha \geq 1$ associated with complete failure. Fig. 3(b) illustrates simulations of damage evolution with $\beta = 0.5$ and $\alpha_0 = 0.1$ under cyclic loading similar to that presented in Fig. 2(b). Since α increases during loading, the transitional strain-invariant ratio ξ_{tran} also increases within the cycle. Therefore, the onset of damage in every cycle depends on the damage level reached in the previous cycle. Fig. 3(b) shows that the onset of damage occurs at stress levels close to the maximal value of the previous cycle. This theoretical result is consistent with the experimental observation of the Kaiser effect (e.g. Holcomb 1993; Lavrov 2001). Fig. 4 illustrates the stable and unstable types of damage evolution under constant loading applied to a rock sample with pre-existing damage $\alpha = 0.1$ and $\beta = 0.5$. Under low differential stress, a steady-state solution of eq. (7) is obtained after about 5500 s for 40 MPa differential stress and after about 7500 s for 80 MPa. The rate of damage evolution goes to zero at these stress levels and the behaviour corresponds to stable weakening. For higher differential stresses, there is unstable weakening associated with accelerated damage increase with time until complete failure. The time-to-failure decreases with increasing differential stress. These results are in qualitative agreement with static fatigue tests discussed by Kranz *et al.* (1982), Lawn (1993), Martin & Chandler (1994) and others.

2.2 Damage-related viscosity

Viscosity values for rocks at room temperature and stresses below the onset of acoustic emissions are above 10^{20} Pa s. With such values of η irreversible deformation, before the complete brittle failure during typical rock mechanics experiments, cannot be attributed to viscous deformation. Previous studies suggested that the observed permanent inelastic deformation before brittle failure is related to effective viscosity associated with the growth of microcracks and frictional sliding between grains (e.g. Lockner 1993, 1998). For sim-

ilar reasons, Martin & Chandler (1994) related the damage variable to irreversible volumetric strain. Here we assume that for $\xi > \xi_{\text{tran}}(\alpha)$ there is a linear relation between the rate of irreversible deformation and the rate of damage accumulation. With this we rewrite (5) as

$$\frac{d\varepsilon_{ij}^{v}}{dt} = \begin{cases} C_v \frac{d\alpha}{dt} \left(\sigma_{ij} - \frac{1}{3}\sigma_{kk}\delta_{ij} \right), & d\alpha/dt > 0 \\ 0, & d\alpha/dt \leq 0. \end{cases} \quad (9)$$

The compliance or inverse of viscosity ($C_v d\alpha/dt$) relates the deviatoric stress to the rate of irreversible strain accumulation. The units of the material parameter C_v are the inverse of stress and there is no new timescale related to its value. The timescale associated with the damage-related viscosity is controlled by the rate of the damage process (7) through the damage rate parameter C_d. The parameter C_v is assumed to be constant and constrained using laboratory data presented in the following section. Here we do not account for irreversible volumetric deformation (inelastic compaction), which is negligible for granite and is small for Berea sandstone under relatively low confining pressures. A damage-related inelastic compaction was discussed by Ricard & Bercovici (2003) and Hamiel *et al.* (2004).

3 ANALYSIS OF LABORATORY DATA

Westerly granite and Berea sandstone have been used extensively in laboratory experiments on brittle deformation because they provide convenient representative material for low-porosity crystalline rock and high-porosity sedimentary rock, respectively. In this section we analyse data obtained during two experiments with Westerly granite, GR1 and GR2, and two experiments with Berea sandstone, BS1 and BS2. The experiment GR1 was conducted and analysed earlier by Lockner *et al.* (1992), where it was referred to as G3. The other three experiments are new to this work. Experiments GR1, GR2 and BS1 were done under a confining pressure of 50 MPa, while BS2 was conducted under a confining pressure of 100 MPa (Table 1). Data recorded in the experiments include differential stress, axial and transverse strain and the acoustic emission (AE) rate. In test GR1 the stress was controlled by a feedback of the AE rates to keep a stable increase of AE events. The loading portions of all other tests were done with a constant shortening rate of the combined piston and rock sample. During tests GR2, BS1 and BS2 the stress was cycled a number of times. Additional explanations of the experimental set-up can be found in Lockner *et al.* (1992).

3.1 Westerly granite

All stress–strain curves recorded in the experiments with the Westerly granite samples clearly show two different regimes of deformation. The stress–strain data exhibit an almost linear relation until the onset of acoustic emissions and significant deviation from linear elasticity with the onset of AE (see Figs 5 and 8). We use the linear part of the stress–strain curves to calculate the initial elastic moduli (λ, μ_0) for samples GR1 and GR2 (see Table 1 for all model coefficients). The measured axial and transverse strains

Table 1. Model coefficients for the different experiments.

Sample	Rock type	P_{conf} (MPa)	λ (10^4 MPa)	μ_0 (10^4 MPa)	ξ_0	β	C_d (s^{-1})	C_v (10^{-5} MPa^{-1})
GR1	Westerly granite	50	2.9	1.9	−0.56	0	3.0	2.0
GR2	Westerly granite	50	3.0	2.3	−0.62	0.15	2.2	3.0
BS1	Berea sandstone	50	0.5	1.4	−0.8	0.5	50	10
BS2	Berea sandstone	100	0.5	1.4	−1.0	0.5	50	10

throughout the experiment allow us also to estimate the transitional strain-invariant ratio (ξ_{tran}) at the onset of acoustic emissions. The parameters C_d and C_v for GR1 and GR2 are estimated by fitting the calculated stress–strain curves to the observed ones. The accumulated irreversible strain estimated from the small loading cycles of sample GR2 provides additional constraint for C_v.

Fig. 5 shows the measured differential stress versus axial strain of GR1 together with the calculated curves. Simulations with a homogeneous damage distribution (single-element) using the elastic damage model with $\beta = 0$, ignoring irreversible strain accumulation ($C_v = 0$) and a different kinetic coefficient ($C_d = 3$ and 5 s^{-1}) do not fit well with the observed data over the entire deformation range (Fig. 5a). The discrepancy near the peak stress can be attributed to the accumulation of relatively high irreversible strain at this stage. A better fit near the peak stress can be obtained with a single-element simulation that accounts for the accumulation of irreversible strain, using $C_v = 2 \times 10^{-5}$ MPa^{-1} and $C_d = 3$ s^{-1} (Fig. 5b). These results indicate the importance of the damage-related viscosity for reproducing correctly the experimental data. A small remaining discrepancy between the observed and simulated stress–strains may be related to the strong damage localization at the final stages of damage evolution. This localization, shown by acoustic emission locations
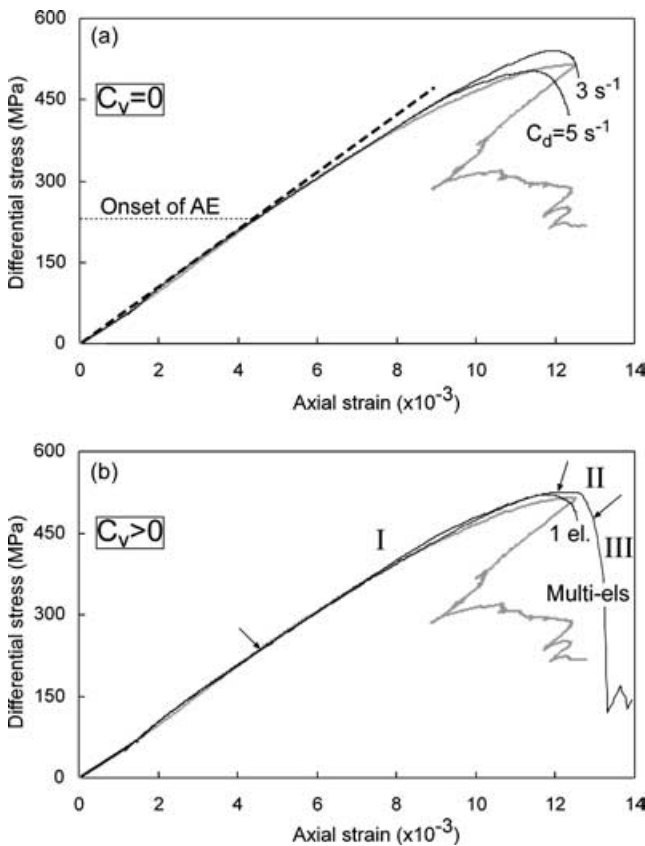
(Lockner *et al.* 1992), is a common feature of granite sample fracturing and requires 3-D calculations that account for heterogeneity of damage distribution. The simulation results in Fig. 5(b) with multi-elements in a cylinder governed by the viscoelastic damage rheology model provide a better fit to the observed data (see the Appendix for details on the numerical method). Fig. 5(b) also shows a comparison between the results obtained with multi-elements and with a single element. The discrepancy between stress–strain curves simulated with multi- and single-element approaches is negligible for most of the simulation, except for the very last stage of deformation where the damage strongly localizes to a narrow zone. This localization is observed in the laboratory experiments just before the peak stress (Lockner *et al.* 1992). Therefore, in the calculations for the other samples (GR2, BS1 and BS2), we use only a single-element model. In addition to fitting the stress–strains, the 3-D numerical simulation also reproduces the evolving spatial distribution of deformation and damage. The simulated evolution of damage can be divided into three stages, marked on Fig. 5(b), characterized by different spatial distribution. Fig. 6 represents the locations of failed numerical elements at these stages. In stage (I) of the deformation the damage is not localized and the failed elements occupy most of the sample surface. Stage (II) corresponds to the onset of localized damage and stage (III) represents the total final failure along a narrow zone. Fig. 7 shows the numerical grid used in the simulation and the values of the damage variable α for each element at the final stage of the simulation. At that stage a localized damage zone cuts the sample obliquely with an orientation compatible with the observed fault zone orientation in the laboratory experiment (Lockner *et al.* 1992).

The linear viscoelastic damage model with $\beta = 0$ (not shown here) can provide a reasonable fit to the observed data of GR2 except for the small loading cycles. The damage model with $\beta > 0$ improves the fitting quality throughout the loading cycles. Fig. 8 shows comparisons between the measured and calculated stress–strain (axial and transverse) curves for GR2 using $\beta = 0.15$. We note that the β value for the low-porosity granite rock is about zero or relatively small.

Figure 5. (a) Measured stress–strain curve for GR1 (grey line) compared with the calculated curves for single-element simulation, from linear elasticity (dashed line) and the pure elastic damage model ($C_v = 0$) with different C_d (3.0 and 5.0 s^{-1}, black lines). (b) Measured stress–strain curve for GR1 compared with the calculated curves for the viscoelastic damage model ($C_v > 0$) for single-element simulation and multi-element 3-D simulation (black lines). Stages (I, II, III) indicated on the stress–strain curve correspond to failed elements location plots in Fig. 6. Note that the discrepancy between multi- and single-element approaches is negligible until stage II. For model coefficients see Table 1.
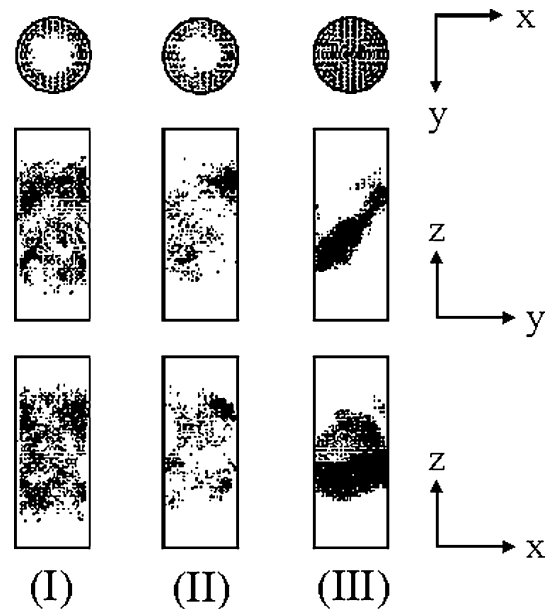

Figure 6. Three stages of spatial distribution of evolving damage from the 3-D numerical simulations. The black dots represent the location of failed numerical elements at each stage.
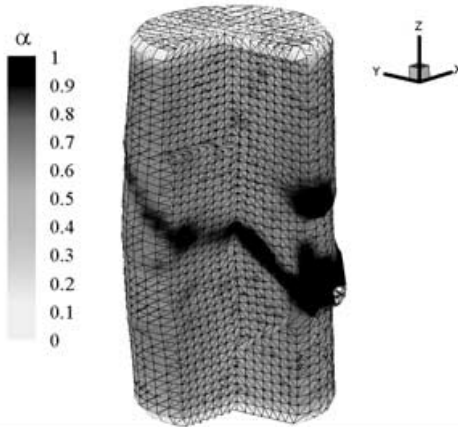
Figure 7. Numerical grid of the sample and the values of the damage variable, α, of each element at the final stage of the simulation.
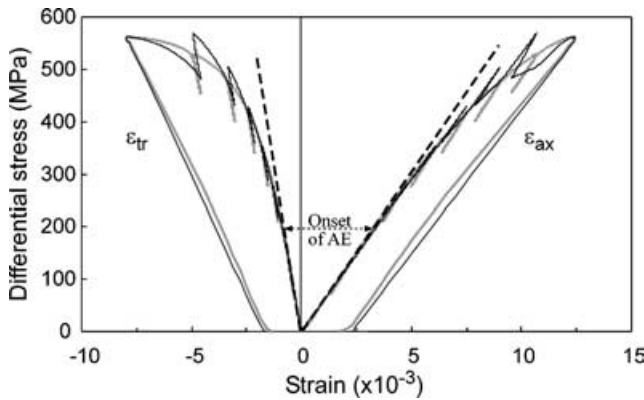

Figure 8. Measured stress–strain curves, axial and transverse, for GR2 (grey line) compared with the calculated curve (black line). For model coefficients see Table 1.

Figure 9. Measured stress–strain curves, axial and transverse, for BS1 (grey line) compared with the calculated curves (black line), with $\beta = 0$ (a) and $\beta = 0.5$ (b). For model coefficients see Table 1.

3.2 Berea sandstone

The Berea sandstone experimental data (Figs 9–11) reveal three fundamental different aspects of deformation from those of the Westerly granite. First, the onset of AE in Berea sandstone samples occurs at a very early stage of the loading and linear elastic deformation is hardly observed. Second, the accumulated inelastic strain during loading is much higher, reaching about a third of the total strain (Figs 9 and 10). Third, throughout all of the unloading–loading cycles acoustic emissions are not recorded (Fig. 11) and inelastic strain is not accumulated (Figs 9 and 10). These features can be accounted for by assigning the Berea sandstone higher values of β and C_v than those of the Westerly granite.

To illustrate the foregoing effects we compare the observed and single-element calculated stress–strain curves for BS1 (at 50 MPa confining pressure) and BS2 (at 100 MPa confining pressure) using the viscoelastic damage model with $\beta = 0$ (Figs 9a and 10a). These calculations show that irreversible strain continues to accumulate during the small cycles of loading–unloading, in contrast to the experimental data. Corresponding model calculations with $\beta = 0.5$ provide a significantly better fit to the observed data (Figs 9b and 10b). In agreement with observed acoustic emissions, the damage onset occurs at a very early stage of deformation and the damage level remains constant during most of the cycles (Fig. 11). This
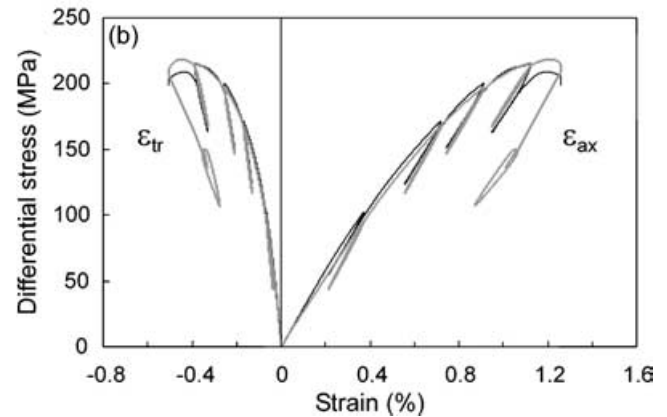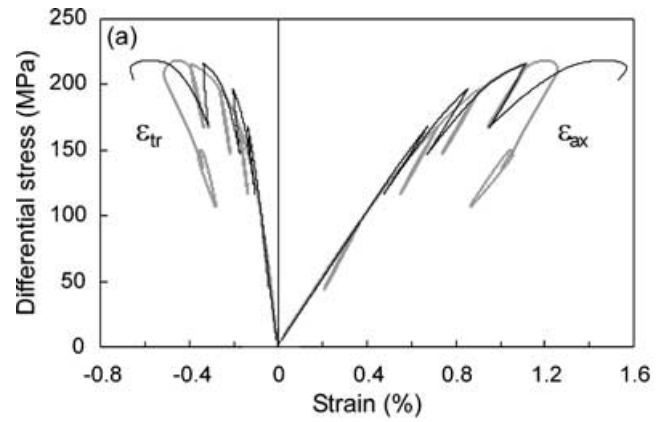
feature is compatible with the observed rock behaviour associated with the Kaiser effect. The model simulations used to fit the data recorded in the two experiments with Berea sandstone (BS1 and BS2) differ only in that for BS1 the employed critical strain-invariant ratio was $\xi_0 = -0.8$, whereas for BS2 it was $\xi_0 = -1$ (Table 1). Hamiel *et al.* (2004) discuss similar changes of ξ_0 in relation to a transition from brittle failure to cataclastic flow in high-porosity rocks.

4 DISCUSSION

4.1 Elastic moduli of the damaged rock

Having limited observational data, Agnon & Lyakhovsky (1995) and Lyakhovsky *et al.* (1997a) assumed previously linear relations between the elastic moduli and the damage variable. In their model, the transition between degradation and healing occurs at a critical strain-invariant ratio ξ_0 related to the friction angle (Agnon & Lyakhovsky 1995). Once the strain field exceeds ξ_0, unstable weakening of the sample occurs. Thus the previous version of the model with linear damage–moduli relation did not account for possible stable weakening, and failed to describe the Kaiser effect. In the new version of the damage rheology model with power-law relations between the damage variable and elastic moduli (eq. 3), the rate of damage evolution (eq. 7) depends on the value of the damage variable itself. Instead of the constant critical strain-invariant ratio separating healing and weakening regions, damage onset occurs at
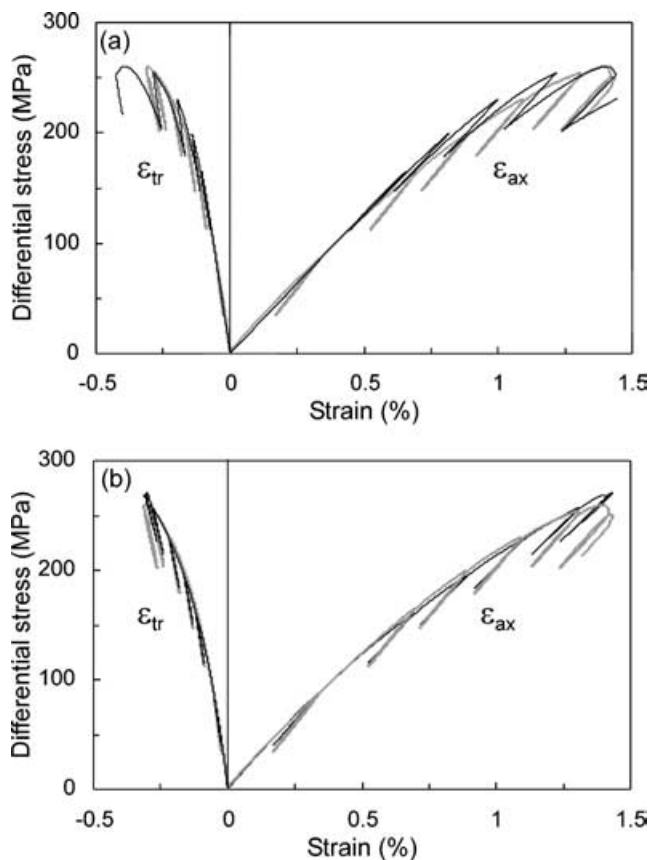
Figure 10. Measured stress–strain curves, axial and transverse, for BS2 (grey line) compared with the calculated curves (black line), with $\beta = 0$ (a) and $\beta = 0.5$ (b). For model coefficients see Table 1.
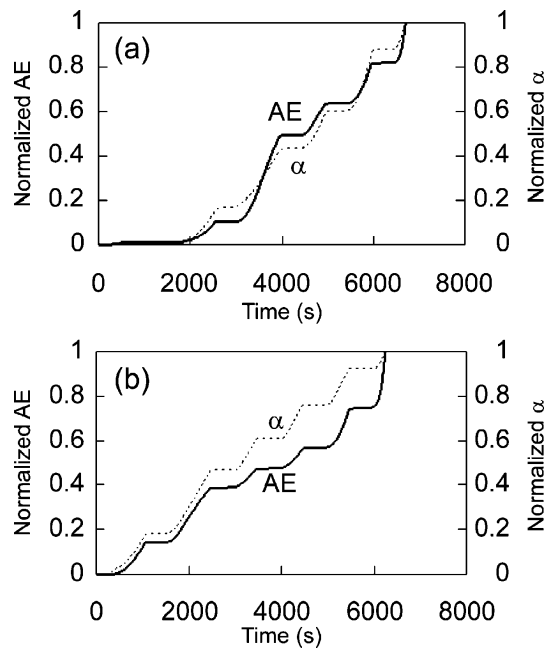

Figure 11. Normalized AE (thick line) compared with normalized damage variable (dotted line) during BS1 (a) and BS2 (b). Note that both accumulated AE and damage are roughly constant during the small unloading–loading cycles.

the transitional strain-invariant ratio ξ_{tran} that increases with growing damage variable. This allows the model to reproduce a transition from stable to unstable fracturing of brittle rocks and the Kaiser effect. Since the transition from degradation to healing depends on the damage level accumulated during a previous loading cycle and the rate of healing is negligibly small on laboratory timescales at room temperature, the damage does not change until the stress of the current loading cycle approaches the maximum stress of the previous cycle (Fig. 3). Similarly to static fatigue tests (e.g. Kranz *et al.* 1982; Lawn 1993; Bolotin 1999) the simulations with the model using power-law moduli–damage relations show decrease in strength with increase in loading time (Fig. 4).

4.2 Damage-related viscosity and irreversible deformation

The elastic damage rheology model of Lyakhovsky *et al.* (1997a) ignores gradual accumulation of irreversible strain that is observed in rock mechanics experiments (e.g. Martin & Chandler 1994) before a macroscopic brittle failure occurs. In the present study, we generalize the Maxwell viscoelasticity and use the concept of damage-related viscosity to model a gradual accumulation of irreversible deformation. The effective compliance or inverse of viscosity in a viscoelastic damage rheology model is proportional to the rate of damage accumulation and vanishes at a state of stress corresponding to healing (negative rate of damage). Under this assumption, short-term damage-related viscous deformation does not exist if there is no damage evolution (since the effective viscosity will be very high).

The concept of damage-related viscosity is supported by the deformation behaviour of rock in the progressive unloading and reloading cycles. In the stress–stain curves of Figs 8–10 we do not observe significant irreversible deformation in the cycles that have low AE rates. Figs 5 and 8–10 show a quantitative agreement between the damage model with a damage-related viscosity and the experimental observations on crystalline as well as high-porosity rock samples.

4.3 Comparisons between the model and new experimental results

The generalized viscoelastic damage rheology model was tested against new laboratory data, two experiments with Westerly granite GR1 and GR2 and two experiments with Berea sandstone BS1 and BS2. The Berea sandstone experimental data (Figs 9–11) reveal three aspects of deformation different from those of the Westerly granite that support the model assumptions. First, the onset of AE in Berea sandstone samples occurs at a very early stage of loading and linear elastic deformation is hardly observed. Second, the irreversible strain in Berea sandstone samples is much higher than in Westerly granite, reaching about a third of the total strain (Figs 9 and 10). Third, throughout all of the unloading–loading cycles acoustic emissions are not recorded (Fig. 11) and irreversible strain is not accumulated (Figs 9 and 10). All these features are well reproduced using a power-law ($\beta = 0.5$) model with damage-related viscosity ($C_v = 1 \times 10^{-4}$ MPa^{-1}). These model coefficients for the Berea sandstone differ significantly from those of the Westerly granite. The model fits well the experimental data of the Westerly granite with small β values, ranging from 0 to 0.15, and $C_v = 2$–3×10^{-5} MPa^{-1}. The comparison between elastic and viscoelastic damage rheology model simulations (Fig. 8) shows that the accumulated irreversible deformation in the Westerly granite sample is on the order of 10 per cent of the total deformation at the peak stress. Thus, the elastic damage rheology model with $\beta = 0$ is a good approximation for

low-porosity crystalline rocks, while a power-law moduli–damage relation and accumulation of irreversible strain is essential for high-porosity rocks.

4.4 3-D numerical simulation of evolving damage

Although a single-element simulation of damage rheology for homogeneous material gives a reasonable fit to the stress–strain curves until failure, it cannot reproduce correctly the evolution in the vicinity of a peak stress and post-failure frictional sliding. This is because single-element simulation does not account for spatial variability of the evolving damage, which can only be done by using a 3-D multi-element simulation. The numerical model correctly reproduces the stress–strain data including macroscopic failure and post-failure frictional behaviour. The location maps of failed elements during the numerical simulation of Westerly granite show a transition from distributed non-localized damage at an initial stage of damage evolution to a localized oblique damage zone at a later stage (Fig. 6). Similarly to localization of plastic deformation in fracture mechanics models (e.g. Rudnicki & Rice 1975), the loss of convexity in the damage rheology model leads to strain localization along the narrow damage zone (Fig. 7). The simulated transition from distributed to localized damage is compatible with geometrical patterns reported for acoustic emission location maps by Lockner *et al.* (1992) for Westerly granite samples.

ACKNOWLEDGMENTS

REFERENCES

Agnon, A. & Lyakhovsky, V., 1995. Damage distribution and localization during dyke intrusion, in *The Physics and Chemistry of Dykes*, pp. 65–78, eds Baer, G. & Heimann, A., Balkema, Rotterdam.

Alm, O., Jaktlund, L.L. & Kou, S., 1985. The influence of microcrack density on the elastic and fracture mechanical properties of Stripa granite, *Phys. Earth planet. Inter.,* **40,** 161–179.

Barenblatt, G.I., 1962. Mathematical theory of equilibrium cracks in brittle fracture, *Adv. Appl. Mech.,* **7,** 55–129.

Bazant, Z.P. & Cedolin, L., 1991. Stability of Structures, *Elastic, Inelastic, Fracture and Damage Theories*, Oxford University Press, New York.

Ben-Zion, Y. & Lyakhovsky, V., 2002. Accelerated seismic release and related aspects of seismicity patterns on earthquake faults, *Pure appl. Geophys.,* **159,** 2385–2412.

Ben-Zion, Y., Dahmen, K., Lyakhovsky, V., Ertas, D. & Agnon, A., 1999. Self-driven mode switching of earthquake activity on a fault system, *Earth planet. Sci. Lett.,* **172,** 11–21.

Bieniawski, Z.T., 1967. Mechanism of brittle fracture of rock, parts I, II and III, *Int. J. Rock Mech. Min. Sci. Geomech. Abstr.,* **4,** 395–430.

Bolotin, V.V., 1999. *Mechanics of Fatigue*, CRC Press, Boca Raton, FL.

Budiansky, B. & O'Connell, R.J., 1976. Elastic moduli of a cracked solid, *Int. J. Solids Struct.,* **12,** 81–97.

Chai, H., 1993. Observation of deformation and damage at the tip of cracks in adhesive bonds loaded in shear and assessment of a criterion for fracture, *Int. J. Fracture,* **60,** 311–326.

Cundall, P.A., 1989. Numerical experiments on localization in frictional materials, *Ing. Arch.,* **59,** 148–159.

Cundall, P.A. & Board, M., 1988. A microcomputer program for modeling large-strain plasticity problems, in *Numerical Methods in Geomechanics: Proceedings of the 6th International Conference on Numerical Methods in Geomechanics, Innsbruck*, pp. 2101–2108, ed. Swoboda, C., Balkema, Rotterdam.

deGroot, S.R. & Mazur, P., 1962. *Nonequilibrium Thermodynamics*, North Holland, Amsterdam.

Dugdale, D.S., 1960. Yielding of steel sheets containing slits, *J. Mech. Phys. Solids,* **8,** 100–104.

Hamiel, Y., Lyakhovsky, V. & Agnon, A., 2004. Coupled evolution of damage and porosity in poroelastic media: theory and applications to deformation of porous rocks, *Geophys. J. Int.,* **156,** 701–713.

Hansen, N.R. & Schreyer, H.L., 1994. A thermodynamically consistent framework for theories of elasticity coupled with damage, *Int. J. Solids Struct.,* **31,** 359–389.

Holcomb, D.J., 1993. Observations of the Kaiser effect under multiaxial stress states: implications for its use in determining *in situ* stress, *Geophys. Res. Lett.,* **20,** 2119–2122.

Huang, W-L., Kunin B. & Chudnovsky, A., 1991. Kinematics of damage zone accompanying curved crack, *Int. J. Fracture,* **50,** 143–152.

Ida, Y., 1972. Cohesive force across the tip of longitudinal shear crack and Griffith's specific surface energy, *J. geophys. Res.,* **77,** 3796–3805.

Jaeger, J.C. & Cook, N.G.W., 1984. *Fundamentals of Rock Mechanics*, Chapman and Hall, New York.

Ju, J.W., 1990. Isotropic and anisotropic damage variables in continuum damage mechanics, *J. Eng. Mech.,* **116,** 2764–2770.

Kachanov M., 1994. On the concept of damage in creep and in the brittle-elastic range, *Int. J. Damage Mech.,* **3,** 329–337.

Kaiser, J., 1950. An investigation into the occurrence of noises in tensile tests or a study of acoustic phenomena in tensile test, *PhD thesis*, Technische Hochschule Munchen, Munich, Germany.

Kranz, R.L., Harris, W.J. & Carter, N.L., 1982. Static fatigue of granite at 200°C, *J. geophys. Res.,* **9,** 1–4.

Lavrov, A., 2001. Kaiser effect observation in brittle rock cyclically loaded with different loading rates, *Mech. Mater.,* **33,** 669–677.

Lawn, B., 1993. *Fracture of Brittle Solids*, 2nd edn, Cambridge University Press, Cambridge.

Lockner, D.A., 1993. Room temperature creep in saturated granite, *J. geophys. Res.,* **98,** 475–487.

Lockner, D.A., 1998. A generalized law for brittle deformation of Westerly granite, *J. geophys. Res.,* **103,** 5107–5123.

Lockner, D.A. & Byerlee, J.D., 1980. Development of fracture planes during creep in granite, in *2nd Conference on Acoustic Emission/Microseismic Activity in Geological Structures and Materials*, pp. 11–25, eds Hardy, H.R. & Leighton, F.W., Trans-Tech Publications, Clausthal-Zellerfeld, Germany.

Lockner, D.A., Byerlee, J.D., Kuksenko, V., Ponomarev, A. & Sidorin, A., 1991. Quasi-static fault growth and shear fracture energy in granite, *Nature,* **350,** 39–42.

Lockner, D.A., Byerlee, J.D., Kuksenko, V., Ponomarev, A. & Sidorin, A., 1992. Observations of quasi-static fault growth from acoustic emissions. in *Fault Mechanics and Transport Properties of Rocks*, International Geophysics Series Vol. 51, pp. 3–31, eds Evans, B. & Wong, T.-F., Academic Press, San Diego, CA.

Lyakhovsky, V.A. & Myasnikov, V.P., 1984. On the behavior of elastic cracked solid, *Phys. Solid Earth,* **10,** 71–75.

Lyakhovsky, V., Ben-Zion, Y., & Agnon, A., 1997a. Distributed damage, faulting, and friction, *J. geophys. Res.,* **102,** 27 635–27 649.

Lyakhovsky, V., Reches, Z., Weinberger., R. & Scott, T.E., 1997b. Nonlinear elastic behavior of damaged rocks, *Geophys. J. Int.,* **130,** 157–166.

Lyakhovsky, V., Ben-Zion, Y. & Agnon, A., 2001. Earthquake cycle, fault zones, and seismicity patterns in a rheologically layered lithosphere, *J. geophys. Res.,* **106,** 4103–4120.

Malvern, L.E., 1969. *Introduction to the Mechanics of a Continuum Medium*, Prentice-Hall, Englewood Cliffs, NJ.

Martin, C.D. & Chandler, N.A., 1994. The progressive fracture of Lac du Bonnet granite, *Int. J. Rock Mech. Min. Sci Geomech. Abstr.,* **31,** 643–659.

Murnaghan, F.D., 1951. *Finite Deformation of an Elastic Solid*, John Wiley, New York.

Nishihara, M., 1957. Stress-strain relation of rocks, *Doshisha Eng. Rev.,* **8,** 32–54.

Palmer, A.C. & Rice, J.R., 1973. The growth of slip surfaces in the progressive failure of overconsolidated clay, *Proc. R. Soc. London*, A,**332,** 527–548.

Pestman, B.J. & Munster, J.G., 1996. An acoustic emission study of damage development and stress—memory effects in sandstone, *Int. J. Rock Mech. Min. Sci. Geomech. Abstr.,* **33,** 585–593.

Poliakov, A., Cundall, P., Podladchikov, Y. & Lyakhovsky, V., 1993. An explicit inertial method for the simulation of viscoelastic flow: an evaluation of elastic effects on diapiric flow in two- and three-layers model, in *Proceedings of the NATO Advanced Study Institute on Dynamic Modeling and Flow in the Earth and Planets,* pp. 175–195, eds Runcorn, K.E. & Stone, D., Kluwer, Dordrecht.

Reches, Z. & Lockner, D.A., 1994. Nucleation and growth of faults in brittle rocks, *J. geophys. Res.,* **99,** 18 159–18 173.

Ricard, Y. & Bercovici, D., 2003. Two-phase damage theory and crustal rock failure: the theoretical 'void' limit, and the prediction of experimental data, *Geophys. J. Int.,* **155,** 1057–1064.

Rubin, A.M., 1993. Tensile fracture of rock at high confining pressure: implications for dike propagation, *J. geophys. Res.,* **98,** 15 919–15 935.

Rubin, A.M., 1995. Why geologists should avoid using 'fracture toughness' (at least for dykes), in *Physics and Chemistry of Dykes*, pp. 53–63, eds Baer, G. & Heimann, A., Balkema, Rotterdam.

Rudnicki, J.W. & Rice, J.R., 1975. Conditions for the localization of deformation in pressure-sensitive, dilatant materials, *J. Mech. Phys. Solids,* **23,** 371–394.

Schock, R.N., 1977. The response of rocks to large stresses, in *Impact and Explosion Cratering*, pp. 657–688, eds Roddy, D.L., Pepin, R.O. & Merrill, R.B., Pergamon Press, New York.

Schock, R.N. & Louis, H., 1982. Strain behavior of a granite and a graywacke sandstone in tension, *J. geophys. Res.,* **87,** 7817–7823.

Tang, C.A., Chen, Z.H., Xu, X.H. & Li, C., 1997. A theoretical model for Kaiser effect in rock, *Pure appl. Geophys.,* **150,** 203–215.

Weinberger, R., Reches, Z. Eidelman, A. & Scott, T.S., 1994. Tensile properties of rocks in four-point beam tests under confining pressure, in *Proceedings of the First North American Rock Mechanics Symposium, Austin, Texas,* pp. 435–442, eds Nelson, P. & Laubach, S.E., A.A. Balkema, Rotterdam.

Willemse, E.J.M. & Pollard, D.D., 1998. On the orientation and patterns of wing cracks and solution surfaces at the tips of a sliding flaw or fault, *J. geophys. Res.,* **103,** 2427–2438.

Yukutake, H., 1989. Fracturing process of granite inferred from measurements of spatial and temporal variations in velocity during triaxial deformation, *J. geophys. Res.,* **94,** 15 639–15 651.

Zietlow, W.K. & Labuz, J.F., 1998. Measurement of the intrinsic process zone in rock using acoustic emission, *Int. J. Rock Mech. Min. Sci. Geomech. Abstr.,* **35,** 291–299.

Zoback, M.D. & Byerlee, J.D., 1975. The effect of microcrack dilatancy on the permeability of Western granite, *J. geophys. Res.,* **80,** 752–755.

APPENDIX A: NUMERICAL METHOD

Our 3-D numerical simulations use the fast Lagrangian analysis of continua (FLAC) algorithm (Cundall & Board 1988; Cundall 1989; Poliakov *et al.* 1993). The formulation is explicit in time, using an updated Lagrangian scheme to provide the capability for large strains. The FLAC algorithm is believed to offer advantages over conventional finite-element schemes in cases where material instability occurs. Physical instability is modelled without numerical instability if inertial terms are included in the equilibrium equations. The general procedure basically involves solving a force balance equation for each grid point in the body

$$\frac{\partial v_i}{\partial t} = \frac{F_i}{m}, \tag{A1}$$

where v_i and F_i are velocity and force applied to a node of mass m. The solution of the equations of motion provides velocities at each grid point, which are used to calculate element strains. These strains substituted into the linear or non-linear constitutive relation provide element stresses and then forces acting on the element faces. These forces recalculated to the grid nodes are the necessary input for the solution of the equation of motion in the next step of the calculation cycle.

The computational mesh consists of four-point tetrahedral elements. The four linear element basic functions, L_k ($k = 1$–4 being the number of element nodes) are

$$L_k = a_k + b_k x_1 + c_k x_2 + d_k x_3, \tag{A2}$$

where a_k, b_k, c_k, d_k are constants and (x_1, x_2, x_3) are coordinates within the element. These shape functions are used to linearly interpolate the nodal velocities ($V_i^{(k)}$) within each element and enable calculation of the strain increments $\Delta \varepsilon_{ij}$

$$\Delta \varepsilon_{ij} = \Delta t \sum_{k=1}^{4} \left(V_i^{(k)} \frac{\partial L_k}{\partial X_j} + V_j^{(k)} \frac{\partial L_k}{\partial X_i} \right). \tag{A3}$$

After the elastic strains are calculated, the stress tensor is computed using constitutive relation (2), which in our case also includes the local value of the level of damage in the specific element. The nodal forces are now a vector sum of one-third of the forces acting on all faces adjacent to the node:

$$F_i \sum_{\text{faces}} \frac{1}{3} \sigma_{ij} n_j + m g_i, \tag{A4}$$

where n_j is a normal vector to the face, node mass m is one-third of the mass of elements adjacent to the node, and g_i is the gravity acceleration vector. Once the forces are known, new velocities are computed by integrating (A1) over a given time step

$$V_i^{(n)}(t + \Delta t) = V_i^{(n)}(t) + \left[F_i^{(n)} - \chi \left| F_i^{(n)} \right| \text{sign} \left(V_i^{(n)} \right) \right] \times \frac{\Delta t}{m_{\text{inert}}}. \tag{A5}$$

During the integration, the previously calculated force ($F_i^{(n)}$) is damped. The damping term is proportional to the acceleration (out-of-balance) force and sign opposite to velocity with the damping factor $0 < \chi < 1$. This term dissipates the energy of the system and attenuates elastic waves travelling in the simulated area. It vanishes if the system is in equilibrium and provides a convergence of numerical procedure to a steady-state solution. Following Poliakov *et al.* (1993) we use 'inertial' mass in (A5) instead of 'gravity' mass in (A1) to allow adaptive time scaling. The time step, which provides stability to the numerical scheme, is:

$$\Delta t = \frac{1}{2} \frac{\Delta x}{V_p}, \tag{A6}$$

where Δx is a minimal distance between gridpoints and V_p is the maximum possible seismic velocity in the material. Introducing density scale factor ($m_{\text{inert}} = D_s m$) we decrease V_p as the square root of D_s and proportionally increase the time step without any numerical artefacts. This certainly can only be done if the system is close to equilibrium (out-of-balance force approaches to zero). This adaptive procedure, starting with $D_s = 1$, automatically increases D_s if the system is in a steady-state regime, or brings it back to unity if the solution deviates from static.

The damage variable (α) for each element is calculated for every numerical cycle according to eq. (4) with the time step defined by adaptive procedure. If damage in one element achieves its critical level ($\alpha = \alpha_{cr}$) then a drop in stress occurs. The real dynamic process, wherein the stress drop generates waves, is not simulated here. However, a quasi-dynamic procedure is applied to simulate propagation of a rupture front. This is accomplished by recalculating the stress field after each stress drop for every element involved in the rupture process, and by incorporating dynamic weakening of material; the latter is achieved by reducing the critical value of the damage variable, α_{cr}, to $\alpha_{dynamic}$:

$$\alpha_{dynamic} = \alpha_{cr} - \sqrt{\tau_a \frac{d\alpha}{dt}}, \tag{A7}$$

where τ_a is material coefficient.